Catalysis Science & Technology

ROYAL SOCIETY OF CHEMISTRY

PAPER

View Article Online
View Journal | View Issue

Check for updates

Cite this: *Catal. Sci. Technol.*, 2025, 15, 2175

Design and catalytic performance investigation of the Ni–N–C catalyst for CO_2RR: a theoretical study†

Yiming Sun, Xiaoyu Wang, Zhuofan Wu, Anmin Liu and Xuefeng Ren *

Received 18th November 2024,
Accepted 22nd January 2025

DOI: 10.1039/d4cy01394h

rsc.li/catalysis

The combustion of fossil fuels is increasingly contributing to global warming. The recycling of CO_2 plays a crucial role, and the creation of a highly efficient electrocatalyst is essential for enhancing the efficiency of the reaction. This work focused on the theoretical design of Ni–N–C catalysts with different coordination environments of Ni through quantum chemical calculations and analyzed the differences between the coordination environments of pyridine N and pyrrole N on the performance of catalytic CO_2 reduction to CO in order to identify the most efficient catalyst configuration. The Ni–N bonding energy of the catalyst with a vacancy was greater than that of the catalyst without a vacancy, and the activation ability of Ni-pyridine N_2C_1–C was the best. Ultimately, examining various catalysts for converting CO_2 into CO revealed that Ni-pyridine N_2C_1–C exhibited the most effective catalytic impact. In contrast to the energy barrier ΔG = 2.9903 eV in the absence of a catalyst, the energy barrier ΔG = −1.4029 eV during the CO_2 to CO catalytic reaction decreased by 4.3932 eV. This decrease was the largest among all the catalysts mentioned above, and the reaction could be spontaneous from a thermodynamic perspective. The research results provide a theoretical reference for the experimental preparation of catalysts for CO_2 to CO conversion and the resource utilization of CO_2.

1 Introduction

Post industrial revolution, swift advancements in fossil fuel technology have emitted substantial quantities of carbon dioxide (CO_2) for energy, intensifying the urgency of achieving carbon neutrality.[1,2] Consequently, the primary emphasis is on carbon capture and utilization, making the advancement of CO_2 reduction a widespread issue in both academic circles and society at large.

In CO_2RR, the electrocatalyst promotes the conversion of carbon dioxide into various "high-value" products with the help of electricity,[3] involving the transfer of six or more electrons during the electrocatalytic reaction. In these CO_2RR processes, C_1 products (such as methane (CH_4) and methanol (CH_3OH)), C_2 products (such as ethylene (C_2H_4), acetic acid (CH_3COOH), and ethanol (C_2H_5OH)), and C_3 products (such as *n*-propanol (C_3H_8O) and acetone (C_3H_5O)) are formed. The activity and selectivity of the electrocatalyst for reduction products are mainly oriented towards C_1 products, mainly CO and $HCOO^-$, rather than the highly reduced C_1 and polycarbon (C_{2+}) products. CO is the main component of syngas and gas, the main part of C1 compounds, which can also be used as a reducing agent in the metal smelting industry. Therefore, catalysts that catalyze CO_2RR to produce CO are explored in this paper. Compared to photocatalysis,[4] electrocatalytic CO_2 reduction avoids the critical problem of catalyst deactivation due to electron–hole complexation. Currently, scientists have explored a variety of catalysts that perform well,[5] such as pure metal catalysts,[6–10] alloy catalysts,[11] porous material catalysts,[12–17] atomically dispersed metal-based catalysts,[18–22] and metal oxide catalysts.[23] However, monometallic catalysts have limited performance.[24–26] The adsorption properties of alloy catalysts are influenced by interactions between neighboring metal atoms, and porous material catalysts can regulate electrolyte diffusion and generate a volume gradient, thus affecting local alkalinity and improving the selectivity of CO_2RR. Still, they suffer from problems, such as low conductivity, poor stability, and lack of mesoporosity. The M–N–C catalysts have a lower cost than precious metal catalysts, and the metal sites generate a charge accumulation effect, which is favorable for CO_2 chemisorption and provides good selectivity for CO generation. Different central metal ions have distinct electronic structures, geometrical configurations and d-orbital energy levels, so selecting suitable central metal elements is crucial for improving the electrocatalytic ability of M–N–C materials by optimizing surface adsorption. Among them, transition metal elements and main group elements

School of Chemical Engineering, Ocean and Life Sciences, Dalian University of Technology, Panjin 124221, China. E-mail: renxuefeng@dlut.edu.cn

† Electronic supplementary information (ESI) available. See DOI: https://doi.org/10.1039/d4cy01394h

exhibit good electrocatalytic ability when acting as center metal ions (Fe, Co, Ni, Cu, Zn, Mn, Sn and Sb). Integrating transition metal nickel into the N–C substance markedly enhances the catalytic efficiency of CO_2RR. Computational models indicate that incorporating single-atom Ni lowers the energy barrier for reactions in CO_2RR. Once the atomically scattered Ni was secured to the carbon substance, the single-atom Ni demonstrated peak atomic usage, augmented the concentration of active sites, and enhanced the catalytic efficiency of CO_2RR. Alterations in the d-orbital energy state of the central metal ion occurred as it was encircled by distinct neighboring ligands, suggesting that modifying the coordination setting of the central metal ion might control the electronic configuration of the M–N–C substance. Changes in the coordination environment can alter the nitrogen atom species by changing the coordination number of the nitrogen atoms. Good catalytic activity for CO_2RR compared to other M–N_x structures, such as M–N_2, M–N_3, and M–N_5,[27,28] most M–N_4 structures, were more selective for CO in CO_2RR.[29–31]

Nitrogen atoms can cause positive charge aggregation,[32] making C adjacent to N the active site for electrocatalytic CO_2RR. Guo[33] conducted a methodical study on the activation capabilities and specificity of N-doped carbon catalysts in electrocatalytic CO_2RR processes. Numerous M–N–C catalysts are known to be employed in the electrocatalytic process of CO_2RR. Jia *et al.*[34] synthesized a single-atom Ni catalyst SA-NiNG-NV with N vacancies possessing higher CO_2RR selectivity. Cheng *et al.*[35] synthesized a large number of Ni–N–C catalytic materials at the edges of the sites by applying microwave stripping, which exhibited extremely high activity in the electrocatalytic CO_2RR process. Wang *et al.*[36] systematically investigated single-atom catalysts with typical transition metals as active sites, and they found that the selectivity in CO_2–CO conversion was ranked as Ni > Co > Fe, and the reactivity was ranked as Co > Ni > Fe. Ni-doped catalysts had high catalytic efficiency, good stability and low price, so this study was aimed at Ni–N–C catalysts. Altering the electron configuration of the coordination center M consequently impacts its location on the active site and the catalyst's specificity. Zhao's team[37] discovered through DFT analysis that pyrrole N predominantly generated HCOOH during CO_2RR catalysis, exhibiting the minimal overpotential of 0.24 V compared to other N-doped graphene types, while Wu[38] ascertained that pyridinium N, as the primary catalyst, effectively converted CO_2 into CO, demonstrating superior catalytic efficiency in theoretical terms.

Consequently, this study conducts theoretical analyses of the stability, CO_2 adsorption stability, and catalytic efficiency of each catalyst using the DMol^3 module in Materials Studio (MS) software. This was performed to evaluate the impact of various coordination settings, including the quantity and nature of nitrogen atom coordination and adsorption type, on the CO_2 reduction efficiency of the Ni–N–C catalysts, and to identify catalysts with superior performance that could inform the use of Ni–N–C catalysts in CO_2RR. DFT calculations can predict and guide experimental design, thereby conserving human and material resources while more effectively screening for catalysts with superior performance. Additionally, DFT enables a deeper understanding of reaction mechanisms.

2 Models and methods

Quantum chemical calculations can be used to design the required catalysts directly on MS software and calculate and predict their catalytic performance, which can reduce the time and workload required for experiments. Many repetitive tasks can be avoided, research efficiency can be improved, and the experimental cost can be reduced, which can provide references and guidance for experiments.

The 5 × 4 graphene was intercepted for reconfiguration, which retained the structural characteristics and reduced the computation. The establishment of the Ni–N–C catalyst model was completed, and geometry optimization was performed by selecting calculation in the DMol^3 module, selecting geometry optimization in the task module in the set up tab, and selecting customized in the quality module. Under the generalized gradient approximation (GGA), the functional chosen was selected as the Perdew–Burke–Ernzerhof (PBE) function, and the basis set with a double-valued atomic orbital plus polarization function (DNP) was chosen to describe the atomic orbitals. The energy convergence criteria, maximum force, and maximum displacement were set during geometry optimization at 2 × 10^{-5} Ha, 0.004 Ha Å^{-1}, and 0.005 Å, respectively. To accelerate electron convergence, the smearing was set to 0.005 Ha. The maximum number of iterations was set to 1000 in more, with medium selected for overall accuracy. The max SCF cycle was set to 1000, and the COSMO solution environment was used with water selected as the solvent. The energy calculation was also done using the DMol^3 module. The binding energy E_B of the catalyst was calculated according to the following formula to select the catalyst configuration with the best stability.

$$E_B = E_{total} - E_{carrier+Ni}, \quad (1.1)$$

where E_b is the average bond energy of the Ni–N bond. The average bond energy is calculated as follows:

$$E_b = E_B \div n, \quad (1.2)$$

where n is the number of Ni–N bonds.

Next, the structure optimization of the Ni–N–C–CO_2 structure was carried out. The structure-optimized CO_2 was attached to the active center, and the parameters were set for structure optimization considering single-site adsorption, double-site adsorption and different atoms connected. The specific equations for calculating adsorption energy are as follows:

$$E_{ads} = E_a - E_{CO_2} - E_{total}. \quad (1.3)$$

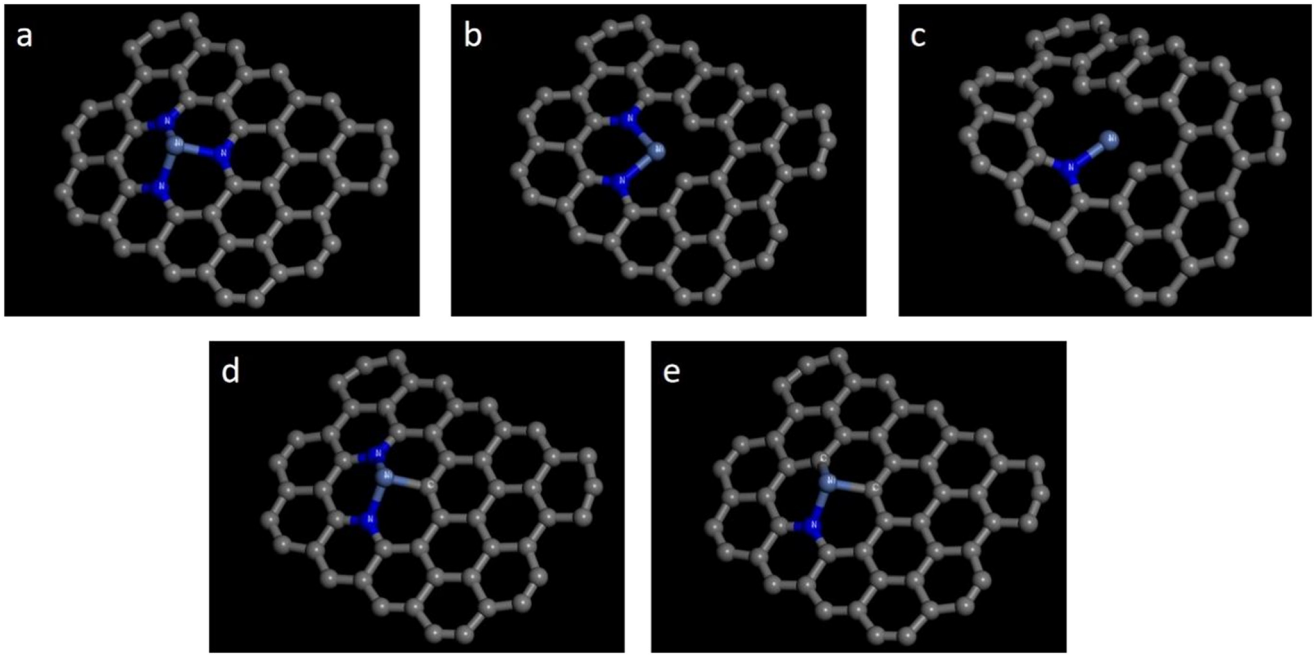

Fig. 1 Five configurations of Ni-pyridine N_nV_{3-n}–C catalysts: (a) Ni-pyridine N_3–C; (b) Ni-pyridine N_2V_1–C; (c) Ni-pyridine N_1V_2–C; (d) Ni-pyridine N_2C_1–C; and (e) Ni-pyridine N_1C_2–C.

Ultimately, the Gibbs free energies for the CO_2 reduction to CO reaction intermediates, both catalyzed and uncatalyzed, were determined.

3 Results and discussion

3.1 Ni–N–C catalyst design

3.1.1 Ni-Pyridine N–C catalyst design. Ni-Pyridine N_nV_{3-n}–C catalysts were Ni–N–C catalysts with three pyridine N atoms anchoring Ni and containing vacancies. Each N atom formed a pyridine structure with a six-membered ring with C atoms, and the Ni atoms were not out of the same plane as the graphene C atoms, as shown in Fig. 1.

Ni-Pyridine N_nV_{4-n}–C catalysts were Ni–N–C catalysts consisting of four pyridine N atoms anchored to Ni atoms and containing vacancies, and each N atom formed a six-membered ring with graphene C in a pyridine structure. Fig. 2 illustrates that the Ni-pyridine N_nV_{4-n}–C catalysts can be categorized into seven configurations.

3.1.2 Ni-Pyrrole N–C catalyst design. Ni-Pyrrole N_nV_{4-n}–C catalysts were Ni–N–C catalysts consisting of four pyrrole N atoms anchored to Ni atoms and containing vacancies, and each N atom formed a five-membered ring with graphene C in a pyrrole structure. The Ni-pyrrole N_nV_{4-n}–C catalysts can be categorized into seven configurations, as shown in Fig. 3.

3.2 Stability studies of Ni–N–C catalysts

The Ni-pyridine N_nV_{3-n}–C catalyst was taken as an example, and the study calculated the average bond energies of the Ni–N and Ni–C bonds for each configuration. The results are presented in Table 1. Among the five structures, the one with the largest bond energy was the Ni-pyridine N_2V_1–C catalyst, which had an average bond energy of −0.0898 eV of the Ni–N bond, indicating that the catalyst had good stability. The largest total bond energy was the d structure, the Ni-pyridine N_2C_1–C catalyst, which was anchored by two N atoms and one C atom, with a total summed energy of E_B = −0.1796 eV, showing good stability. In summary, the stable structures of the Ni-pyridine N_nV_{3-n}–C catalysts were Ni-pyridine N_2V_1–C and Ni-pyridine N_2C_1–C.

3.3 Effect of the number of vacancies on the performance of Ni–N–C catalysts

Subsequently, the catalysts underwent examination for the most occupied molecular orbital (HOMO) and the lowest unoccupied molecular orbital (LUMO). Both HOMO and LUMO symbolize the primary levels of molecular orbital energy. HOMO symbolizes the most filled molecular orbitals, while LUMO denotes the least occupied molecular orbital. For the energy band gap $\Delta E = E_{LUMO} - E_{HOMO}$, the rate of electron movement within the catalyst can be ascertained using ΔE. A reduced ΔE indicates a quicker electron transfer rate in the front molecular orbitals and a more catalytic catalyst.

The frontline molecular orbital energy levels and ΔE of the three previously selected Ni–N–C catalysts are illustrated in Fig. 4–6. Compared to the catalysts without vacancies, the catalysts containing vacancies were significantly larger for ΔE. The ΔE of the Ni-pyridine N_3V_1–C catalyst with vacancies was 0.872 eV, which was more than three times larger than that of the Ni-pyridine N_4–C catalyst without vacancies (ΔE = 0.278 eV).

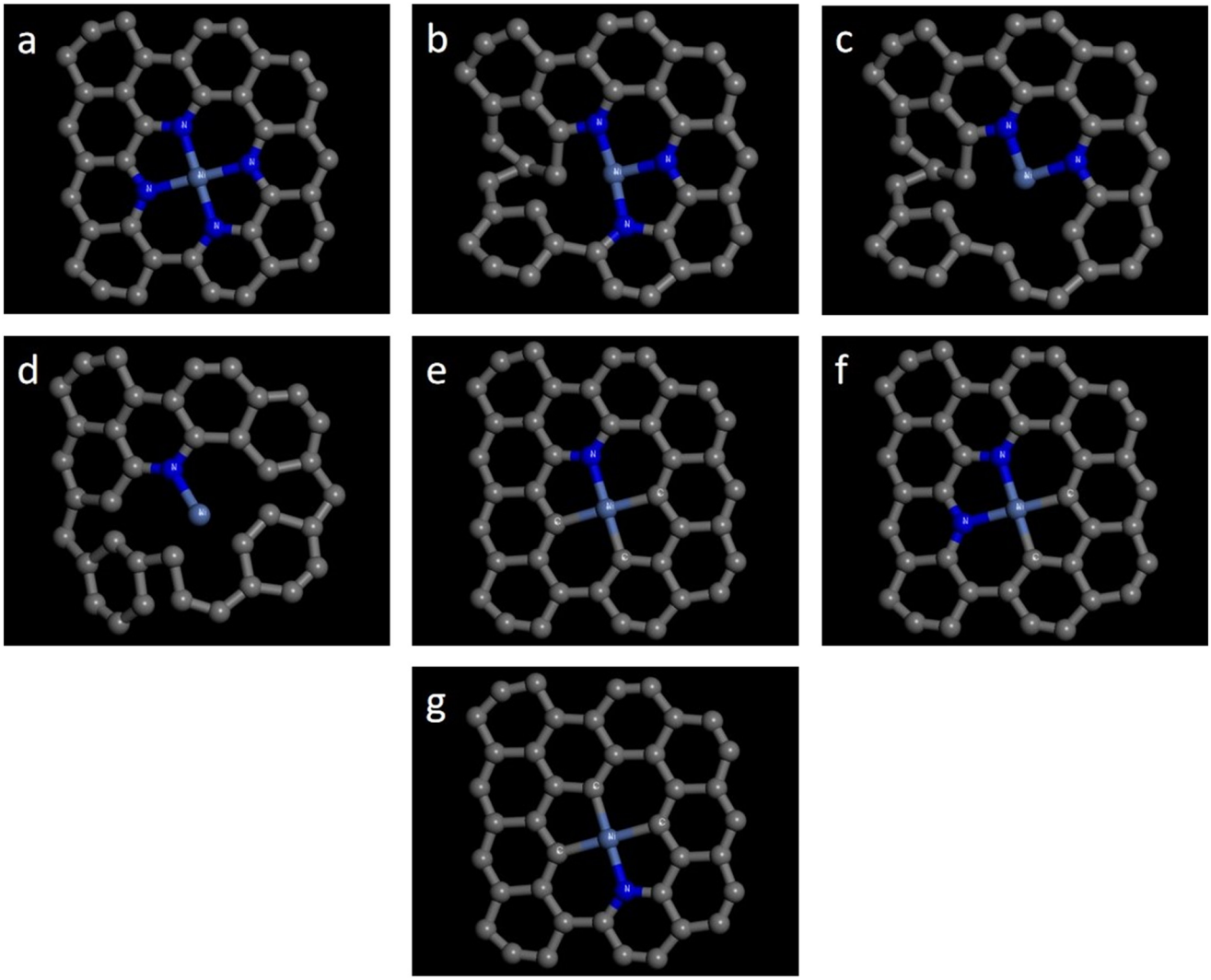

Fig. 2 Seven structures of Ni-pyridine N_nV_{4-n}–C catalysts: (a) Ni-pyridine N_4–C; (b) Ni-pyridine N_3V_1–C; (c) Ni-pyridine N_2V_2–C; (d) Ni-pyridine N_2V_1–C; (e) Ni-pyridine N_3C_1–C; (f) Ni-pyridine N_2C_2–C; and (g) Ni-pyridine N_1C_3–C.

3.4 Study of CO_2 adsorption capacity of Ni–N–C catalysts

All atoms of the Ni-pyridine N_2V_1–C catalyst, Ni-pyrrole N_2V_2–C catalyst and Ni-pyridine N_1V_3–C catalyst were in the same plane, so there was no need to consider the direction of CO_2 binding to the catalyst during structure optimization. Only single-site and double-site adsorption, as well as Ni–C bonding and Ni–O bonding, must be considered for a total of three cases.

The Ni atoms of the Ni-pyridine N_2C_1–C catalyst and the Ni-pyridine N_1V_3–C catalyst were not in the same plane as the carrier graphene. Therefore, not only single-site and double-site adsorption but also the direction of CO_2 molecule adsorption had to be considered, so there were 6 cases.

3.4.1 Active site analysis of Ni–N–C catalysts. The global activity analysis was carried out in the previous section using the front molecular orbital energy levels. Next, the active sites of the catalysts were determined using Fukui indices.

Table 2 demonstrates the Fukui functions for each Ni–N–C catalyst Ni atom as well as the N and C atoms attached to the Ni atom. From the table, it can be observed that the $f(+)$ and $f(-)$ of the Ni atoms of the six catalysts were the maximum values within the catalyst, indicating that this site could react with both Lewis acids and Lewis bases. Taking catalyst Ni-pyridine N_2C_1–C Catalyst Ni–C N–O as a case study, a periodic cell (Fig. S4†) was constructed, and the Fukui indices of all atoms were summarized in Table S1.† Therefore, it was the most suitable catalyst site.

Table 3 showed the Fukui index of CO_2, from which it could be observed that the C atom of CO_2 had the largest $f(+)$ and a greater positron density, so in single-site adsorption, it could be assumed that the stability of the C atom connected to the Ni atom of the catalyst was greater than that of the O atom connected to the Ni atom. Therefore, the Ni–O connection was not considered for the time being.

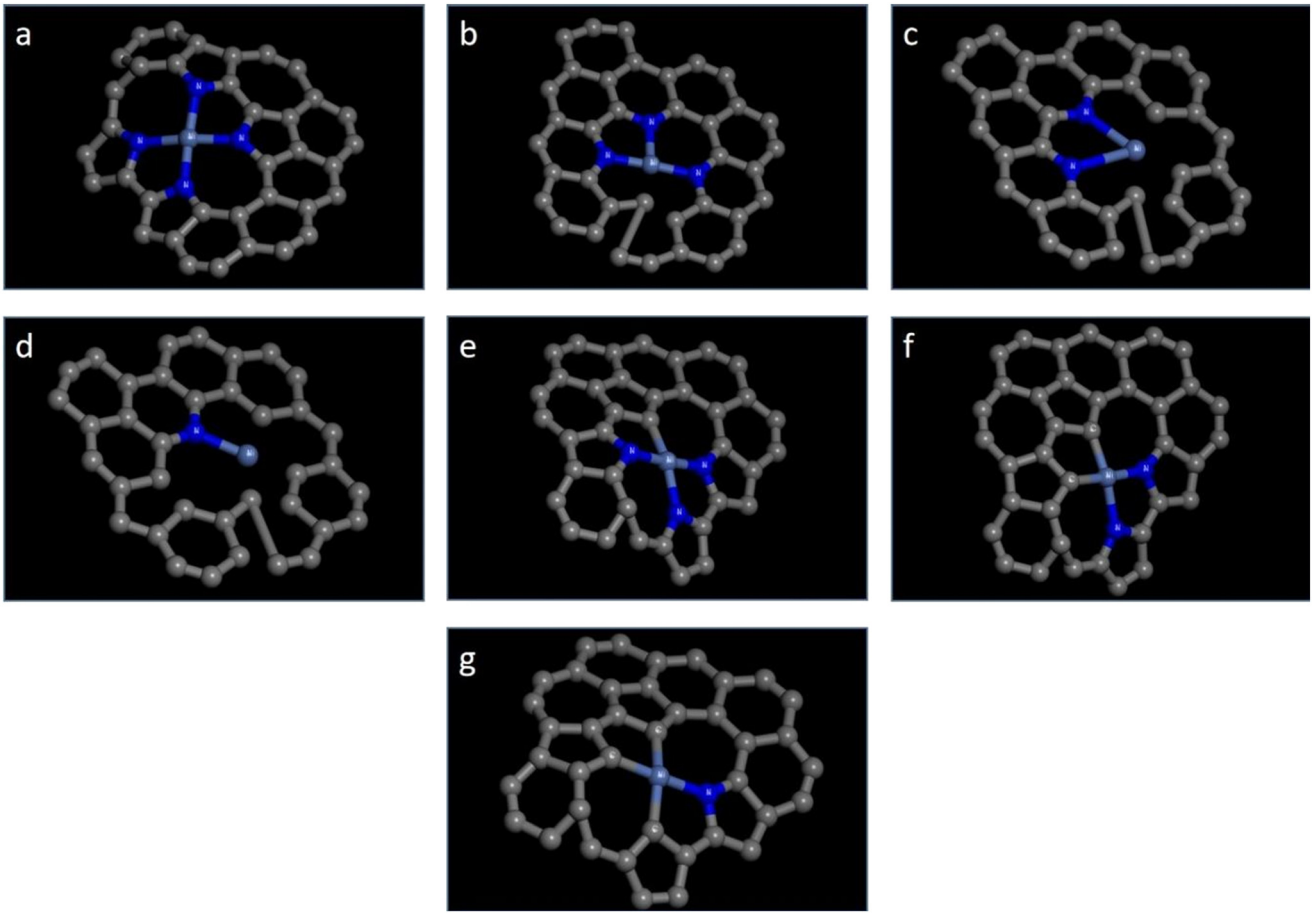

Fig. 3 Seven structures of Ni-pyrrole N_nV_{4-n}–C catalysts: (a) Ni-pyrrole N_4–C; (b) Ni-pyrrole N_3V_1–C; (c) Ni-pyrrole N_2V_2–C; (d) Ni-pyrrole N_2V_1–C; (e) Ni-pyrrole N_3C_1–C; (f) Ni-pyrrole N_2C_2–C; and (g) Ni-pyrrole N_1C_3–C.

3.4.2 Stability study of CO_2 adsorption over Ni–N–C catalysts. Next, six selected Ni–N–C catalysts with good stability were determined for adsorption stability.

(1) Ni-Pyridine N_2V_1–C catalysts. The structure of the Ni–N_2V_1–C–CO_2 intermediate was designated (Fig. S1†). The bond lengths, bond angles and adsorption energies of the Ni–N_2V_1–C–CO_2 structure were shown in Table 4.

As shown in Table 4, the binding energies of (a) and (b) were negative and (c) was positive. Therefore, (c) CO_2 could not be stabilized for adsorption. The C═O bond lengths of (a) were 1.178 Å and 1.179 Å, respectively, which were not much changed compared to the CO_2 bond length of 1.178 Å. The C═O bond lengths of (c) were both 1.178 Å, and there was no change in the bond lengths, so (a) and (b) had a low activation effect on CO_2.

Table 1 Bond energies of Ni-pyridine N_nV_{3-n}–C catalysts

Isomers	$E_{carrier+Ni}$/eV	E_{total}/eV	E_B/eV	E_b/eV
a	−3536.73	−3536.87	−0.1481	−0.0494
b	−3481.98	−3482.16	−0.1796	−0.0898
c	−3427.27	−3427.31	−0.0500	−0.0500
d	−3520.02	−3520.20	−0.1798	−0.0599
e	−3503.39	−3503.54	−0.1511	−0.0504

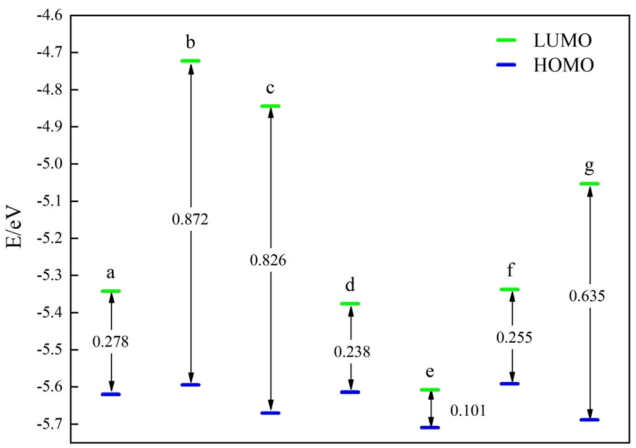

Fig. 4 Frontline molecular orbital energy levels and ΔE for Ni-pyridine N_nV_{4-n}–C catalysts: (a) Ni-pyridine N_4–C; (b) Ni-pyridine N_3V_1–C; (c) Ni-pyridine N_2V_2–C; (d) Ni-pyridine N_2V_1–C; (e) Ni-pyridine N_3C_1–C; (f) Ni-pyridine N_2C_2–C; and (g) Ni-pyridine N_1C_3–C.

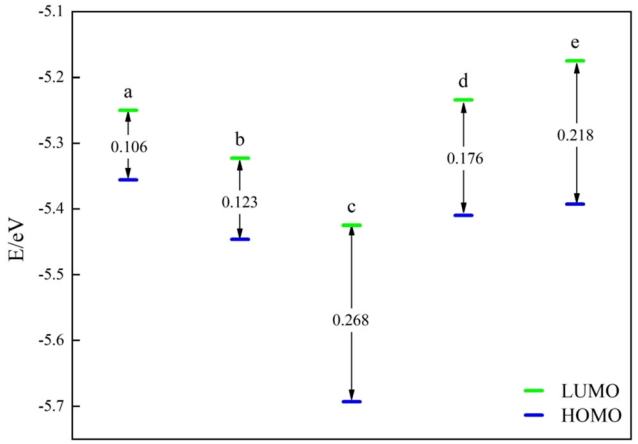

Fig. 5 Frontline molecular orbital energy levels and ΔE for Ni-pyridine N_nV_{3-n}–C catalysts: (a) Ni-pyridine N_3–C; (b) Ni-pyridine N_2V_1–C; (c) Ni-pyridine N_1V_2–C; (d) Ni-pyridine N_2C_1–C; and (e) Ni-pyridine N_1C_2–C.

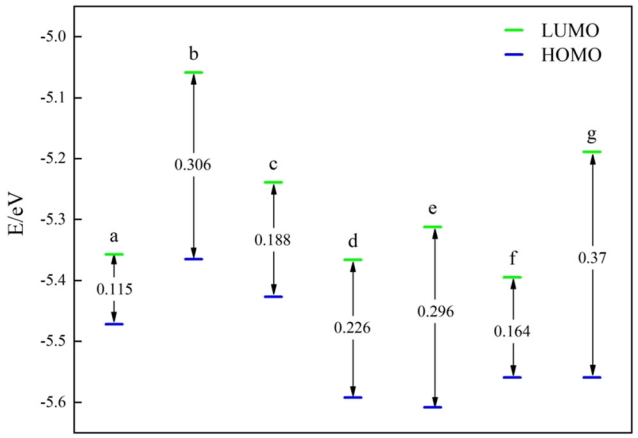

Fig. 6 Frontline molecular orbital energy levels and ΔE for Ni-pyrrole N_nV_{4-n}–C catalysts: (a) Ni-pyrrole N_4–C; (b) Ni-pyrrole N_3V_1–C; (c) Ni-pyrrole N_2V_2–C; (d) Ni-pyrrole N_2V_1–C; (e) Ni-pyrrole N_3C_1–C; (f) Ni-pyrrole N_2C_2–C; and (g) Ni-pyrrole N_1C_3–C.

Table 3 Fukui index for CO_2 catalysts

	$f(+)$		
	Atom	Mulliken	Hirshfeld
Ni-Pyrrole N_1C_3–C	C(1)	0.462	0.384
	O(2)	0.269	0.308
	O(3)	0.269	0.308

Table 4 Adsorption energies and bond lengths of Ni-pyridine N_2V_1–C–CO_2 intermediates

Isomers	E_{ads}/eV	d_{C-O1}/Å	d_{C-O2}/Å
a	−0.0092	1.178	1.179
b	−0.0087	1.178	1.178
c	0.0045	1.178	1.178

(2) Ni-Pyridine N_2C_1–C catalysts. The bond lengths, bond angles and adsorption energies of the Ni-pyridine N_2C_1–C–CO_2 structure (Fig. 7) are presented in Table 5.

As shown in Table 5, the adsorption energies of the six structures were negative, so all were stable. The adsorption energies of the three structures where CO_2 was adsorbed from the side close to the Ni atom were significantly more stable. In terms of bond lengths, the structures in which CO_2 was adsorbed from the side close to the Ni atom had a larger change in d_{C-O}, which had a good activation effect on CO_2 molecules.

(3) Ni-Pyridine N_1V_3–C catalysts. The structure of the Ni-pyridine N_1V_3–C–CO_2 intermediate is shown in Fig. S2.† The bond lengths, bond angles and adsorption energies of the Ni-pyridine N_1V_3–C–CO_2 intermediate are illustrated in Table 6.

In terms of binding energy, the binding energies E_{ads} of (a), (b) and (c) were lower than the energy required for CO_2 to be adsorbed stably, and the adsorption of CO_2 was more stable from the side close to Ni atoms than that from the side

Table 2 Fukui index for Ni–N–C catalysts

	$f(+)$			$f(-)$		
	Atom	Mulliken	Hirshfeld	Atom	Mulliken	Hirshfeld
Ni-Pyridine N_2V_1–C	Ni(26)	0.050	0.030	Ni(26)	0.055	0.030
	N(25)	0.002	0.011	N(25)	0.002	0.010
	N(31)	−0.000	0.008	N(31)	0.000	0.008
Ni-Pyridine N_2C_1–C	Ni(26)	0.044	0.036	Ni(26)	0.055	0.030
	N(25)	0.005	0.013	N(25)	0.005	0.013
	N(31)	0.000	0.007	N(31)	0.000	0.007
	N(53)	0.011	0.013	N(53)	0.011	0.013
Ni-Pyridine N_1V_3–C	Ni(39)	0.053	0.030	Ni(39)	0.049	0.030
	N(19)	0.002	0.012	N(19)	0.001	0.012
	C(7)	0.002	0.012	C(7)	0.017	0.012
	C(20)	0.015	0.015	C(20)	0.016	0.015
Ni-Pyrrole N_2V_2–C	Ni(40)	0.076	0.039	Ni(40)	0.069	0.040
	N(19)	0.001	0.013	N(19)	0.000	0.013
	N(20)	0.002	0.014	N(20)	0.002	0.014
Ni-Pyrrole N_1V_3–C	Ni(39)	0.067	0.036	Ni(39)	0.065	0.037
	N(19)	0.003	0.014	N(19)	0.003	0.014
	C(7)	0.0018	0.014	C(7)	0.018	0.014
	C(20)	0.015	0.014	C(20)	0.015	0.014

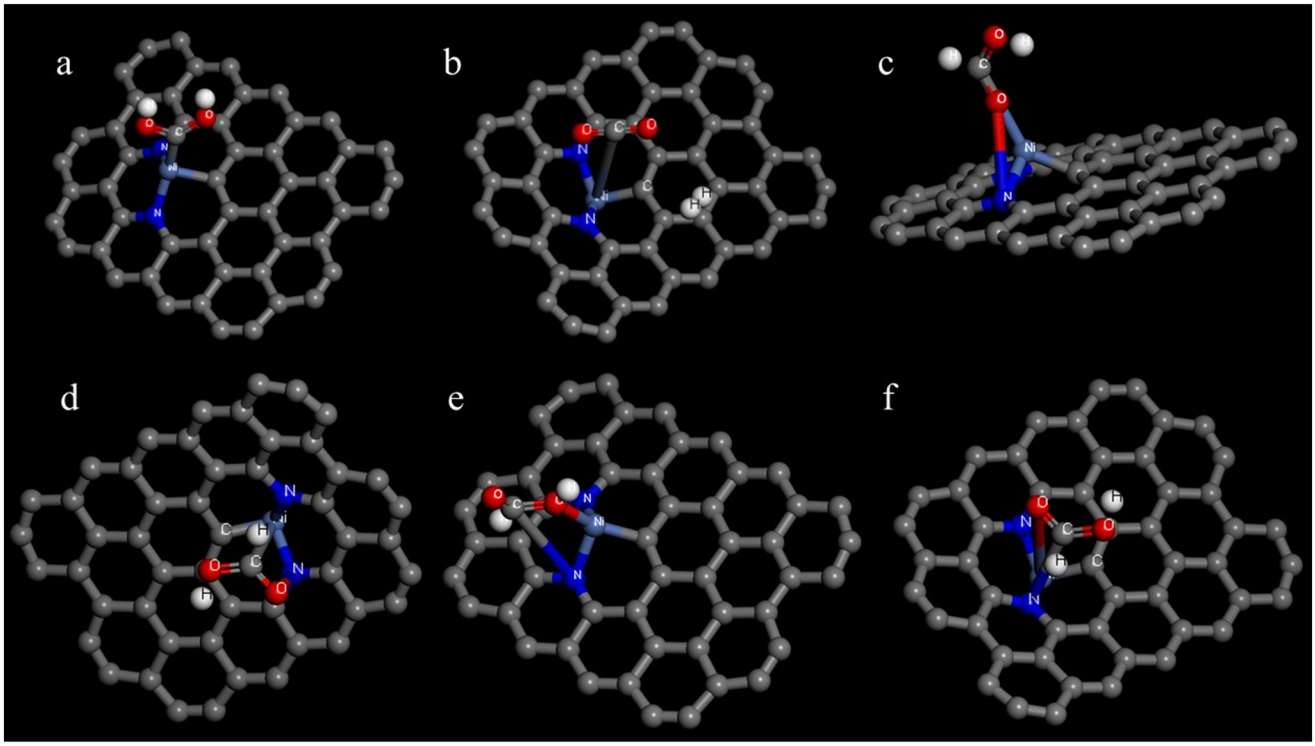

Fig. 7 Isomers of the Ni-pyridine N_2C_1–C–CO_2 intermediate: (a) Ni-pyridine N_2C_1–C–CO_2 single-site adsorption A; (b) Ni-pyridine N_2C_1–C–CO_2 single-site adsorption B; (c) Ni-pyridine N_2C_1–C–CO_2 Ni–C N–O double-site adsorption A; (d) Ni-pyridine N_2C_1–C–CO_2 Ni–C N–O double-site adsorption B; (e) Ni-pyridine N_2C_1–C–CO_2 Ni–O N–C double-site adsorption A; and (f) Ni-pyridine N_2C_1–C–CO_2 Ni–O N–C double-site adsorption B.

far away from Ni atoms. In terms of bond lengths, the C═O bond lengths of (a) and (b) were almost unchanged compared to CO_2, so the catalytic activity of CO_2RR might be very low. The C═O bond lengths of (c) were 1.176 Å and 1.180 Å, which had a certain activation effect on CO_2 molecules.

(4) Ni-Pyrrole N_2V_2–C catalysts. The structure of Ni-pyrrole N_2V_2–C–CO_2 is shown in Fig. 8 as follows: (a) single-site adsorption, with Ni atoms attached to C atoms; (b) double-site adsorption, with Ni–C and N–O bonded; and (c) double-site adsorption, with N–O and N–C bonded. The binding energies and bond lengths of the Ni-pyrrole N_2V_2–C–CO_2 intermediates are illustrated in Table 7.

In terms of binding energy, the binding energies of all three intermediates were negative, so all CO_2 could be stably adsorbed on the catalyst. According to the C═O bond lengths, the three intermediates did not change much compared with CO_2. Therefore, the activation of CO_2 molecules of the Ni-pyrrole N_2V_2–C catalysts was low.

(5) Ni-Pyrrole N_1V_3–C catalysts. Fig. S3† depicts the isomers of the Ni-pyrrole N_1V_3–C–CO_2 intermediate as follows: (a) single-site adsorption, with the Ni atom attached to the C atom; (b) double-site adsorption, with Ni–C and N–O bonded; and (c) double-site adsorption, with N–O–N–C bonded. The binding energies and bond lengths of the Ni-pyrrole N_1V_3–C–CO_2 intermediate are shown in Table 8.

As illustrated in Table 8, the binding energies of all three structures were negative, so CO_2 could be stably adsorbed on the catalysts. However, the C═O bond lengths of (a), (b) and (c) were all 1.178 Å, which was the same as that of CO_2. Therefore, the activation of CO_2 molecules by the three catalysts was low.

3.5 Study of the catalytic activity of catalysts for CO_2RR catalyzation

3.5.1 Analysis of the catalytic activity of CO_2RR by single-site adsorption on catalysts. First, the Ni-pyridine N_2C_1–C

Table 5 Adsorption energies and bond lengths of Ni-pyridine N_2C_1–C–CO_2 intermediates

Isomers	E_{ads}/eV	d_{C-O1}/Å	d_{C-O2}/Å
a	−0.0171	1.166	1.188
b	−0.0088	1.178	1.178
c	−0.0204	1.166	1.186
d	−0.0089	1.177	1.178
e	−0.0198	1.166	1.186
f	−0.0085	1.177	1.178

Table 6 Adsorption energies and bond lengths of Ni-pyridine N_1V_3–C–CO_2 intermediates

Isomers	E_{ads}/eV	d_{C-O1}/Å	d_{C-O2}/Å
a	−0.0084	1.178	1.179
b	−0.0008	1.178	1.178
c	−0.0093	1.176	1.180
d	0.0039	1.178	1.178
e	0.0027	1.177	1.179
f	0.0018	1.177	1.178

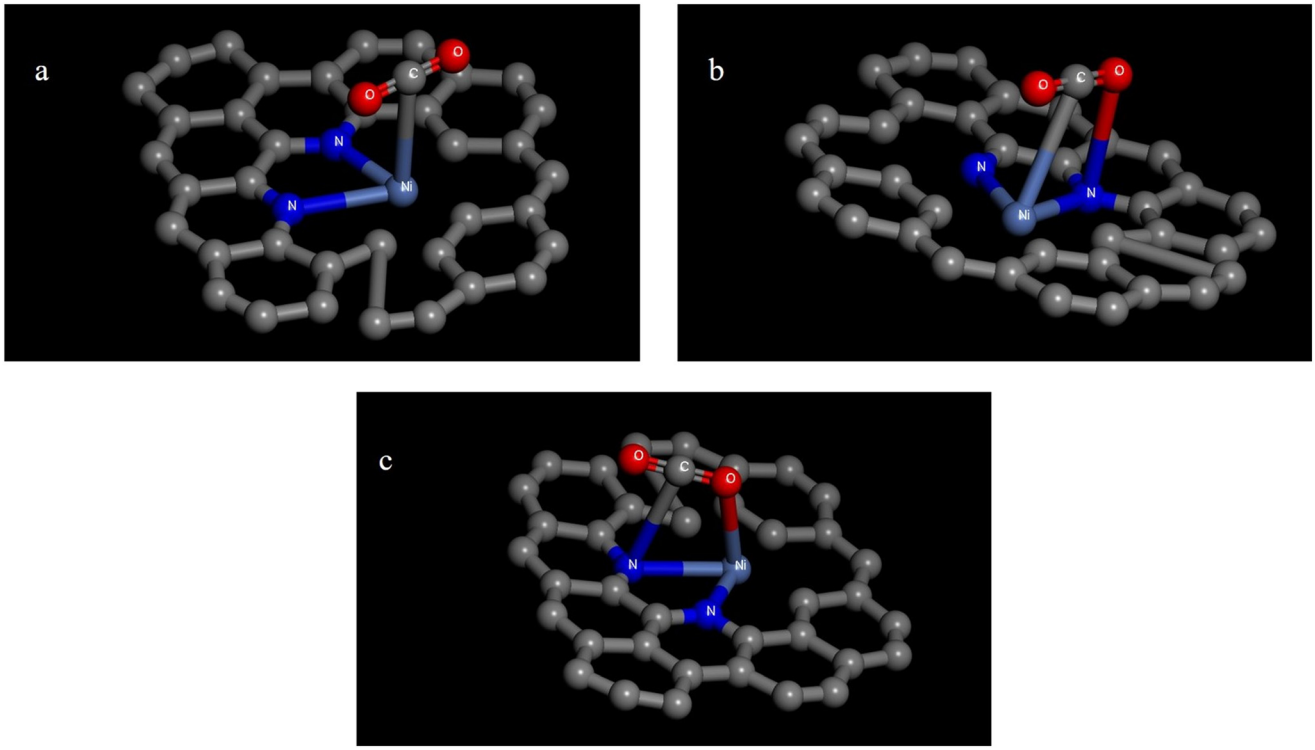

Fig. 8 Isomers of the Ni-pyrrole N_2V_2–C–CO_2 intermediate: (a) Ni-pyrrole N_2V_2–C–CO_2 single-site adsorption; (b) Ni-pyrrole N_2V_2–C–CO_2 Ni–C N–O double-site adsorption; and (c) Ni-pyrrole N_2V_2–C–CO_2 Ni–O N–C double-site adsorption.

catalysts were analyzed for single-site adsorption of CO_2. The adsorption energy data were summarized in Table S2.† The reaction paths of the five catalysts for CO_2 to CO under single-site adsorption were illustrated in Fig. 9. In the same case of single-site adsorption, Ni-pyridine N_1V_3–C catalyst A had the best catalytic effect, with a reaction energy barrier ΔG of 0.2714 eV, which was 2.7189 eV lower than that without catalyst (ΔG = 2.9903 eV). Thus, the catalyst exhibited excellent catalytic performance. The energy barriers of the reaction under Ni-pyridine N_2C_1–C catalyst A decreased by 2.6280 eV and under Ni-pyridine N_2C_1–C catalyst B decreased by 2.5789 eV, both of which had good catalytic performance. The energy barriers of the reaction under Ni-pyridine N_1V_3–C catalyst B, ΔG = 0.7259 eV, compared to that of the reaction without the catalyst, ΔG = 2.9903 eV, decreased by 2.2644 eV, which had some catalytic activity.

Based on the magnitude of the energy barriers, it could be observed that the decisive step for the uncatalyzed and Ni-pyridine N_1V_3–C catalyst B was the formation of *CO, and the rest of the decisive step was the formation of *COOH in the first step.

3.5.2 Analysis of the catalytic activity of CO_2RR by catalyst two-site adsorption. CO_2 can be categorized as Ni–C, N–O bonded and N–O, N–C bonded for two-site adsorption on catalysts, so the same catalyst had two different structures in the same two-site adsorption case.

The catalytic ability of the Ni-pyridine N_2C_1–C catalyst for two-site adsorption of CO_2 from the proximal side with Ni–C, N–O bonding was first investigated. The adsorption energy data were summarized in Table S2.†

Five cases of catalyst two-site adsorption of CO_2 were illustrated in Fig. 10. As observed from the figure, the Ni-pyridine N_2C_1–C catalyst Ni–C N–O A was the best catalyst with a reaction energy barrier of ΔG = −1.4029 eV, which was a decrease of 4.3932 eV compared to the energy barrier of ΔG = 2.9903 eV in the absence of the catalyst, and the reaction was exothermic and thermodynamically capable of proceeding spontaneously. The energy barrier for the reaction under Ni-pyridine N_2C_1–C catalyst Ni–O N–C B was 0.4084 eV, and the energy barrier of the reaction under Ni-pyridine N_2C_1–C catalyst Ni–C N–O B was 1.9764 eV. There was a substantial decrease in the energy barrier compared to the reaction without the

Table 7 Adsorption energies and bond lengths of Ni-pyrrole N_2V_2–C–CO_2 intermediates

Isomers	E_{ads}/eV	d_{C-O1}/Å	d_{C-O2}/Å
a	−0.0093	1.177	1.179
b	−0.0096	1.177	1.178
c	−0.0094	1.178	1.178

Table 8 Adsorption energies and bond lengths of Ni-pyrrole N_1V_3–C–CO_2 intermediates

Isomers	E_{ads}/eV	d_{C-O1}/Å	d_{C-O2}/Å
a	−0.0090	1.178	1.178
b	−0.0101	1.178	1.178
c	−0.0099	1.178	1.178

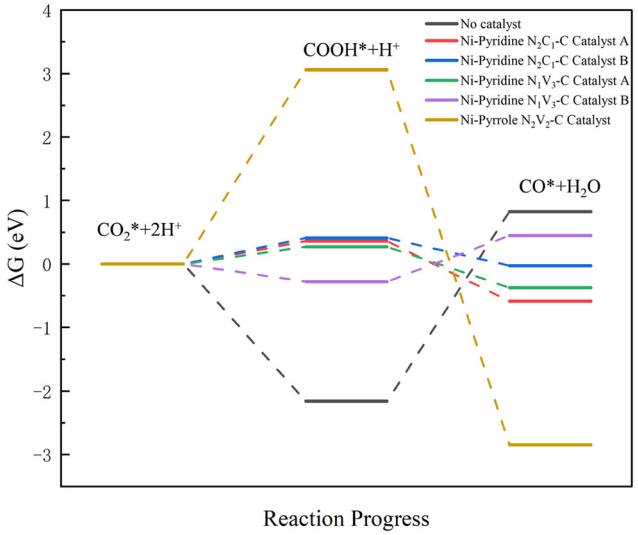

Fig. 9 Reaction path diagram for catalysts in the case of single-site adsorption (where A represents adsorption from the proximal side and B represents adsorption from the distal side).

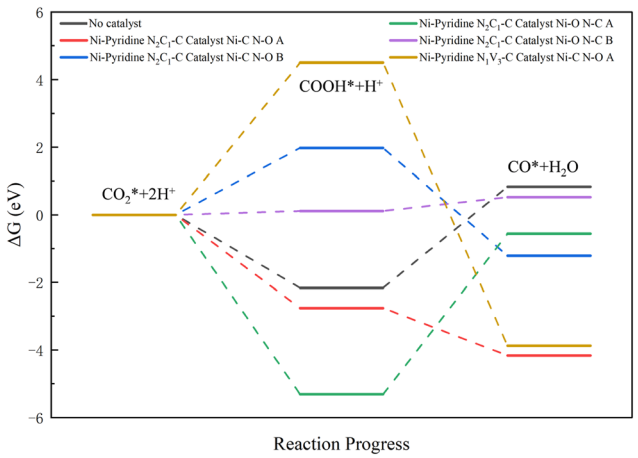

Fig. 10 Reaction path diagram for catalysts in the case of two-site adsorption (where A represents adsorption from the near side and B represents adsorption from the far side).

catalyst, so both had good catalytic activity; the rest of the catalysts had limited catalytic performance.

4 Conclusions

In this study, the stability, activation and catalytic performance of the catalysts were analyzed and screened for better catalysts by performing energy calculations and structure optimization of the constructed structures based on the theoretical basis of quantum chemistry. The following conclusions were obtained.

(1) Vacancies could significantly affect the catalyst properties. The Ni–N–C catalyst with vacancies had a higher Ni–N bond energy and good catalyst stability. However, its ΔE was larger, and the electron conduction rate was slower than that of the catalyst without vacancies. The ΔE of the Ni-pyridine N_3V_1–C catalyst was 0.872 eV, which was more than three times that of the catalyst without the Ni-pyridine N_4–C catalyst with ΔE = 0.278 eV.

(2) The catalysts with excellent activation performance for CO_2 were screened as Ni-pyridine N_2C_1–C catalyst, Ni-pyridine N_1V_3–C catalyst and Ni-pyrrole N_2V_2–C catalyst. Among them, the best CO_2 activation ability was the Ni-pyridine N_2C_1–C catalyst.

(3) In single-site adsorption, the best catalytic effect was achieved by Ni-pyridine N_1V_3–C catalyst A, with reaction ΔG = 0.2714 eV. In two-site adsorption, the best catalytic effect was achieved by Ni-pyridine N_2C_1–C Ni–C N–O A, with reaction ΔG = −1.4029 eV, and the reaction was able to proceed thermodynamically and spontaneously.

(4) Both single-site adsorption and dual-site adsorption reduced the reaction energy barrier compared to no catalyst. Overall, most of the catalytic activities of single-site adsorption were better than those of dual-site adsorption.

Data availability

The data used to support the findings of this paper are included within the article.

Conflicts of interest

There are no conflicts to declare.

Acknowledgements

Supports of the Hefei Advanced Computing Center for this work are gratefully acknowledged.

References

1 L. Tang, R. Ii and K. Tokimatsu, *et al.*, Development of human health damage factors related to CO_2 emissions by considering future socioeconomic scenarios, *Int. J. Life Cycle Assess.*, 2018, **23**, 2288–2299.
2 J. Zhang, J. Shen and L. Xu, *et al.*, The CO_2 emission reduction path towards carbon neutrality in the Chinese steel industry: A review, *Environ. Impact Assess. Rev.*, 2023, **99**, 107017.
3 Y. Zhang, X. Fan and X. He, *et al.*, Ambient electrosynthesis of urea from carbon dioxide and nitrate over Mo_2C nanosheet, *Chin. Chem. Lett.*, 2024, **35**(8), 109806.
4 X. Gao, H. He and W. Zhu, *et al.*, Continuously Flow Photothermal Catalysis Efficiently CO_2 Reduction Over S-Scheme 2D/0D Bi_5O_7I-OVs/$Cd_{0.5}Zn_{0.5}S$ Heterojunction with Strong Interfacial Electric Field, *Small*, 2023, **19**(12), 2206225.
5 S. Jin, Z. Hao and K. Zhang, *et al.*, Advances and Challenges for the Electrochemical Reduction of CO_2 to CO: From

Fundamentals to Industrialization, *Angew. Chem., Int. Ed.*, 2021, **60**(38), 20627–20648.
6 B. Mohanty, S. Basu and B. K. Jena, Transition metal-based single-atom catalysts (TM-SACs); rising materials for electrochemical CO_2 reduction, *J. Energy Chem.*, 2022, **70**, 444–471.
7 Z. Wang, K. Sun and C. Liang, *et al.*, Synergistic Chemisorbing and Electronic Effects for Efficient CO_2 Reduction Using Cysteamine-Functionalized Gold Nanoparticles, *ACS Appl. Energy Mater.*, 2019, **2**(1), 192–195.
8 E. L. Clark, S. Ringe and M. Tang, *et al.*, Influence of Atomic Surface Structure on the Activity of Ag for the Electrochemical Reduction of CO_2 to CO, *ACS Catal.*, 2019, **9**(5), 4006–4014.
9 J. Bonin, A. Maurin and M. Robert, Molecular catalysis of the electrochemical and photochemical reduction of CO_2 with Fe and Co metal based complexes. Recent advances, *Coord. Chem. Rev.*, 2017, **334**, 184–198.
10 J. E. Pander, J. W. J. Lum and B. S. Yeo, The importance of morphology on the activity of lead cathodes for the reduction of carbon dioxide to formate, *J. Mater. Chem. A*, 2019, **7**(8), 4093–4101.
11 Z. B. Hoffman, T. S. Gray and K. B. Moraveck, *et al.*, Electrochemical Reduction of Carbon Dioxide to Syngas and Formate at Dendritic Copper–Indium Electrocatalysts, *ACS Catal.*, 2017, **7**(8), 5381–5390.
12 J. Wu, M. Liu and P. P. Sharma, *et al.*, Incorporation of Nitrogen Defects for Efficient Reduction of CO_2 via Two-Electron Pathway on Three-Dimensional Graphene Foam, *Nano Lett.*, 2016, **16**(1), 466–470.
13 N. Yang, S. R. Waldvogel and X. Jiang, Electrochemistry of Carbon Dioxide on Carbon Electrodes, *ACS Appl. Mater. Interfaces*, 2016, **8**(42), 28357–28371.
14 Q. Li, J. Fu and W. Zhu, *et al.*, Tuning Sn-Catalysis for Electrochemical Reduction of CO_2 to CO via the Core/Shell Cu/SnO_2 Structure, *J. Am. Chem. Soc.*, 2017, **139**(12), 4290–4293.
15 Y. Lum, Y. Kwon and P. Lobaccaro, *et al.*, Trace Levels of Copper in Carbon Materials Show Significant Electrochemical CO_2 Reduction Activity, *ACS Catal.*, 2016, **6**(1), 202–209.
16 Q. Li, W. Zhu and J. Fu, *et al.*, Controlled assembly of Cu nanoparticles on pyridinic-N rich graphene for electrochemical reduction of CO_2 to ethylene, *Nano Energy*, 2016, **24**, 1–9.
17 R. Daiyan, W. H. Saputera and Q. Zhang, *et al.*, 3D Heterostructured Copper Electrode for Conversion of Carbon Dioxide to Alcohols at Low Overpotentials, *Adv. Sustainable Syst.*, 2019, **3**(1), 1800064.
18 J. Kim, J. E. Dick and A. J. Bard, Advanced Electrochemistry of Individual Metal Clusters Electrodeposited Atom by Atom to Nanometer by Nanometer, *Acc. Chem. Res.*, 2016, **49**(11), 2587–2595.
19 T. Imaoka and K. Yamamoto, Wet-Chemical Strategy for Atom-Precise Metal Cluster Catalysts, *Bull. Chem. Soc. Jpn.*, 2019, **92**(5), 941–948.
20 Z. Luo, A. W. Castleman and S. N. Khanna Jr., Reactivity of Metal Clusters, *Chem. Rev.*, 2016, **116**(23), 14456–14492.
21 N. Thiyagarajan, D. Janmanchi and Y.-F. Tsai, *et al.*, A Carbon Electrode Functionalized by a Tricopper Cluster Complex: Overcoming Overpotential and Production of Hydrogen Peroxide in the Oxygen Reduction Reaction, *Angew. Chem., Int. Ed.*, 2018, **57**(14), 3612–3616.
22 G. Li and R. Jin, Atomic level tuning of the catalytic properties: Doping effects of 25-atom bimetallic nanoclusters on styrene oxidation, *Catal. Today*, 2016, **278**, 187–191.
23 S. Guo, S. Zhao and X. Wu, *et al.*, A Co_3O_4-CDots-C_3N_4 three component electrocatalyst design concept for efficient and tunable CO_2 reduction to syngas, *Nat. Commun.*, 2017, **8**(1), 1828.
24 X. Wang, Z. Chen and X. Zhao, *et al.*, Regulation of Coordination Number over Single Co Sites: Triggering the Efficient Electroreduction of CO_2, *Angew. Chem., Int. Ed.*, 2018, **57**(7), 1944–1948.
25 S. Liang, L. Huang and Y. Gao, *et al.*, Electrochemical Reduction of CO_2 to CO over Transition Metal/N-Doped Carbon Catalysts: The Active Sites and Reaction Mechanism, *Adv. Sci.*, 2021, **8**(24), 2102886.
26 W. Ju, A. Bagger and G.-P. Hao, *et al.*, Understanding activity and selectivity of metal-nitrogen-doped carbon catalysts for electrochemical reduction of CO_2, *Nat. Commun.*, 2017, **8**(1), 944.
27 F. Pan, H. Zhang and K. Liu, *et al.*, Unveiling Active Sites of CO_2 Reduction on Nitrogen-Coordinated and Atomically Dispersed Iron and Cobalt Catalysts, *ACS Catal.*, 2018, **8**(4), 3116–3122.
28 J. Feng, H. Gao and L. Zheng, *et al.*, A Mn-N_3 single-atom catalyst embedded in graphitic carbon nitride for efficient CO_2 electroreduction, *Nat. Commun.*, 2020, **11**(1), 4341.
29 L. Bai, Z. Duan and X. Wen, *et al.*, Atomically dispersed manganese-based catalysts for efficient catalysis of oxygen reduction reaction, *Appl. Catal., B*, 2019, **257**, 117930.
30 X. Wen, H. Qi and Y. Cheng, *et al.*, Cu Nanoparticles Embedded in N-Doped Carbon Materials for Oxygen Reduction Reaction, *Chin. J. Chem.*, 2020, **38**(9), 941–946.
31 L. Bai, Z. Duan and X. Wen, *et al.*, Atomically dispersed manganese-based catalysts for efficient catalysis of oxygen reduction reaction, *Appl. Catal., B*, 2019, **257**, 117930.
32 P. P. Sharma, J. Wu and R. M. Yadav, *et al.*, Nitrogen-Doped Carbon Nanotube Arrays for High-Efficiency Electrochemical Reduction of CO_2: On the Understanding of Defects, Defect Density, and Selectivity, *Angew. Chem., Int. Ed.*, 2015, **54**(46), 13701–13705.
33 G.-L. Chai and Z.-X. Guo, Highly effective sites and selectivity of nitrogen-doped graphene/CNT catalysts for CO_2 electrochemical reduction, *Chem. Sci.*, 2016, **7**(2), 1268–1275.
34 C. Jia, S. Li and Y. Zhao, *et al.*, Nitrogen Vacancy Induced Coordinative Reconstruction of Single-Atom Ni Catalyst for Efficient Electrochemical CO_2 Reduction, *Adv. Funct. Mater.*, 2021, **31**(51), 2107072.

35 Y. Cheng, S. Zhao and H. Li, *et al.*, Unsaturated edge-anchored Ni single atoms on porous microwave exfoliated graphene oxide for electrochemical CO_2, *Appl. Catal., B*, 2019, **243**, 294–303.
36 C. Wang, X. Hu and X. Hu, *et al.*, Typical transition metal single-atom catalysts with a metal-pyridine N structure for efficient CO_2 electroreduction, *Appl. Catal., B*, 2021, **296**, 120331.
37 Y. Liu, J. Zhao and Q. Cai, Pyrrolic-nitrogen doped graphene: a metal-free electrocatalyst with high efficiency and selectivity for the reduction of carbon dioxide to formic acid: a computational study, *Phys. Chem. Chem. Phys.*, 2016, **18**(7), 5491–5498.
38 J. Wu, M. Liu and P. P. Sharma, *et al.*, Incorporation of Nitrogen Defects for Efficient Reduction of CO_2 via Two-Electron Pathway on Three-Dimensional Graphene Foam, *Nano Lett.*, 2016, **16**(1), 466–470.